## Single Molecule Bioelectronics

Yongki Choi,[1] Gregory A. Weiss,[2] Philip G. Collins[1]

*Department of Physics and Astronomy[1] and Department of Chemistry[2]*
*University of California at Irvine, Irvine, California 92697, United States*

Conceptually, extending the premise of bioelectronic interfaces down to the scale of single molecules is a straightforward goal. In practice, the challenges are purely technological. Single molecule bioelectronic devices would have to involve features much smaller than state-of-the-art semiconductor electronics, and successful design would have unique requirements for sensitivity and stability.

These imposing specifications are balanced by the potential of enormous rewards, because single molecule bioelectronics would be a breakthrough technology for biochemical research and applications. By peering past the ensemble behaviors of traditional characterization, single molecule techniques aim to directly observe the stochastic fluctuations, instantaneous dynamics, and nonequilibrium behaviors that make up a molecule's full functionality. Moreover, single molecule measurements can uncover the unusual reaction trajectories of a genetically mutated protein or a receptor interacting with pharmacological inhibitors. Building a better understanding of the precise roles of proteins in complex biological processes is a grand challenge for biology, biochemistry, and biophysics in the 21st century.

These potential benefits have spurred the development of a variety of single-molecule techniques. Single molecule fluorescence, specifically Förster resonance energy transfer (FRET), has become a standard tool for single molecule biochemistry (*1*). Meanwhile, single molecule bioelectronics has remained elusive, despite the wide-ranging capabilities of modern solid state electronics.

Recently, a very promising architecture for single molecule bioelectronics was demonstrated using carbon nanotube field effect transistors (Figure 1) (*2*). This next-generation, label-free nanocircuit technique successfully recorded the dynamic motions of single biomolecules, enabling the continuous recording of protein function through many thousands of binding events. The reaction kinetics of complex biochemical events were revealed in real-time with molecule-by-molecule precision to illuminate memory effects, dynamic disorder, and processive variability, all of which remain hidden in ensemble measurements (*2-6*).

This chapter reviews the techniques of fabricating and using this new class of bioelectronic devices. The first section describes the nanotube transistors themselves, and the techniques used to generate single molecule devices. The second and third sections describe and demonstrate how the transistors can be used to monitor biomolecular activity. As examples, single molecule recordings are

described using three different enzymes: lysozyme (*2-4*), cAMP-dependent protein kinase (PKA) (*5*), and the Klenow fragment of DNA polymerase I (KF) (*6*). Success with each enzyme demonstrates the chemical versatility of the devices and their promise as a tool for conducting single molecule research. The chapter concludes with a description of the signal transduction mechanisms at work and guiding design rules for creating equally effective nanocircuits using other biomolecules of interest.

## I. Fabrication Of Single Molecule Electronic Devices

I-A. Carbon nanotube devices

The primary electronic component of this architecture is a carbon nanotube conductor and, preferably, a single-walled carbon nanotube (SWNT). SWNTs have a number of unique properties that make them ideally suited for electronic chemical sensing (*7-11*). First, SWNTs are hollow graphitic cylinders that conduct electricity along their outer, exposed surfaces. Second, the atoms in a SWNT are covalently bonded; unlike most metal and semiconductor films, SWNT conductors are mechanically robust, chemically inert, and insensitive to electromigration. And finally, SWNTs are high mobility, quasi-one-dimensional conductors. The charge carriers in a pristine, isolated SWNT scatter very infrequently (the inelastic mean free path is approximately 1 μm at room temperature (*12*)), so the resistance of a SWNT can be a sensitive indicator of additional scattering caused by environmental surface interactions (*13*). The one-dimensionality of SWNTs means that carriers cannot simply redistribute away from such a scattering site, as they do in metal films or even atomically-thin graphene. In a one-dimensional wire, every individual electron that contributes to the electrical current will directly interact with a single scattering site.

Taking advantage of the properties above and making devices that are sensitive to single molecules requires that devices be fabricated from single, isolated, high quality SWNTs. Many techniques exist in the literature for synthesizing SWNTs (*14*), but the most straightforward method of obtaining clean, isolated SWNTs on an electronic substrate is to synthesize them in place using catalyst-assisted chemical vapor deposition (CVD). By using dilute, lithographically-patterned catalysts, research groups worldwide have been able to fabricate and study SWNT electronic properties.

As a specific example, our preferred SWNT CVD method was developed from a protocol established by Jie Liu's research group at Duke University (*15*). For the catalyst, we prepared an organometallic keggin molecule having a $Fe_{30}Mo_{84}$ center cage surrounded by stabilizing ligands. The keggins were soluble in ethanol, and it was straightforward to prepare a dilute and fast-drying solution suitable for spin coating. We applied a 0.1% dilution of saturated solution onto thermally pretreated (700 °C; 300 s), 4" Si wafers. Using a 6" quartz tube CVD furnace, the deposited catalyst clusters were next oxidized (700 °C; air; 600 s) and reduced (940 °C; 520 sccm $H_2$ in 3000 sccm Ar; 300 s) to produce small,

catalytically-active nanoparticles.  When exposed to carbon feedstock (1000 °C; 1000 sccm $CH_4$ + 520 sccm $H_2$, and 3000 sccm Ar; 180 s), these nanoparticles seeded the growth of single, isolated SWNTs. Our conditions resulted in SWNTs laying on the wafer surface with diameters in the range of 1.1 – 1.6 nm, lengths of 10 – 100 μm, and a dilute areal density of approximately 0.01 SWNTs/$\mu m^2$ (*2*).

Thanks to the length of SWNTs, even the lowest resolution photolithography can successfully contact them with metallic electrodes.  We used a 5" lithographic mask to pattern an array of source and drain metal electrodes (separated by 2 to 5 μm) across an entire wafer, randomly contacting individual SWNTs at various positions on the surface.  The contacting metal can be Pt, Au, or Pd, on top of a sticking layer of Ti or Cr.  Undercut bilayer resists (S1808 over LOR-A1, MicroChem) promoted clean interfaces and reproducible electrical characteristics.  After lithography, the source-drain electrode pairs were electrically probed to identify SWNT connections and then imaged by non-contact atomic force microscopy (AFM) to ensure that each device comprised only one SWNT and to discern that the SWNT was free of particulates.

Throughout the SWNT literature, similar devices are almost exclusively referred to as field effect transistors (FETs) .  Typically, Si wafers with thermally-grown $SiO_2$ surfaces are used as device substrates, allowing voltages applied to the Si to electrostatically gate the SWNTs like in conventional metal-oxide-semiconductor FETs (*16*).  The FET nomenclature is somewhat misleading, though, since many SWNTs are not semiconducting but merely sensitive to gating.  Furthermore, the preparation and usefulness of the single biomolecule devices described here does not depend on any conventional FET characteristics so long as the SWNT device conducts electricity.  A Si gate plays no role in the operation of our devices, and useful devices may be fabricated on insulating and optically-transparent substrates like quartz, glass, and even plastic.  Some degree of electrostatic control is helpful for signal reproducibility, but in all of the cases described below this control is achieved by electrically grounding (or biasing) the surrounding electrolyte.

I-B.  Biofunctionalization

Various methods have been developed for coating SWNT devices with biomolecules or other sensitizing materials.  Tailoring such coatings to the dilute limit of one individual molecular attachment has not been previously appreciated.  Our past work has focused on this limit, finding that covalent (*17-20*) and noncovalent (*2-6*) techniques each have their own advantages and disadvantages.  Experimentally (*21, 22*) and theoretically (*23*), covalent attachment schemes are promising and conceptually appealing.  Here, though, we restrict our attention to one particular noncovalent scheme, selected because it has proven reliable and is easy for others to reproduce.  Furthermore, this scheme is general enough that it is immediately applicable to a wide range of biomolecules.

The noncovalent attachment scheme is outlined in Figure 2. Pyrene-maleimide linker molecules serve as bifunctional crosslinking agents for anchoring a molecule of interest to a SWNT (*24*). The pyrene end of the linker takes advantage of strong $\pi$-$\pi$ interactions to adhere itself to the SWNT sidewall (*25, 26*). As a noncovalent attachment, the pyrene introduces some electronic scattering to the SWNT device, but does not otherwise disrupt the SWNT's electronic band structure nor its stability. The maleimide end of the linker is a Michael acceptor functionality, which is widely used in surface biofunctionalization schemes (*24*). Thiolate functional groups can form a stable thioether bond with the maleimide through nucleophilic Michael addition. The reaction covalently attaches any cysteine-containing protein to the SWNT device. Using mutagenesis, proteins can be modified to present only one cysteine on their surface. Thus, the attachment to the SWNT positions the protein in a predictable orientation. Appropriate design of the cysteine location is described in further detail in Section IV below.

Successful biofunctionalization of SWNT devices has proceeded as follows. First, devices were soaked in a solution of pyrene-maleimide linker molecules (1 mM *N*-(1-pyrenyl)maleimide in ethanol) for 30 min without agitation. Next, the devices were washed with 0.1% Tween-20 in ethanol for 30 min with shaking to remove excess pyrene-maleimide. After one rinse cycle, a second, 10-min rinse was performed using the Tween solution diluted by an equal volume of the appropriate buffer solution for the desired protein. Next, devices were soaked in a solution of protein in its active buffer for 60 min without agitation. Thiol-containing buffer components were replaced with tris(2-carboxyethyl)phosphine (TCEP) where necessary to maintain a reducing environment. Finally, devices were washed with buffer and 0.1% Tween-20 for 30 min with shaking to remove nonspecific protein adsorption on the $SiO_2$ surface. Devices were stored in buffer solution until measurements were completed.

I-C. Limiting attachments to single molecules

The successful production of single molecule electronic devices has proven remarkably straightforward. The overall strategy involved two components. First, the 1-nm SWNT diameter predefined an accessible surface area of only 1,000 – 4,000 nm$^2$ on each device. This small area was comparable to what can be defined using state-of-the-art semiconductor lithography, but with SWNTs it was achieved outside of a clean room environment using rudimentary equipment and nonstringent conditions.

Second, this target area was reduced to the footprint of a single molecule using two low-yield, sequential reactions. The density of adhered pyrene linkers can be widely varied, and our pyrene concentration and rinsing has been empirically developed to make the final number of linkers on the SWNT quite dilute. When followed by the low-yield Michael addition reaction, the two-step biofunctionalization resulted in an average attachment yield of only one protein per μm of SWNT length.

This average spacing was approximately proportional to the concentration of protein used during the final incubation. For a particular protein, the final number of attachments could be easily increased or decreased by factors of two or three.

The procedure for testing a new protein attachment typically involved performing the complete biofunctionalization protocol on a number of SWNTs in parallel. Using AFM imaging to count protein attachments, we empirically determined the attachment probability and then adjusting the incubation concentration and time appropriately. Alternately, a different optimization scheme modified the length of exposed SWNT conductor. Generally, SWNT devices were initially coated with a layer of polymer or oxide to minimize electronic fluctuations and protect the metal electrodes from electrolyte solutions. This protective layer was then selectively removed, using electron beam or optical lithography, to expose a short portion of the SWNT conductor to the experimental solutions. In this manner, the lengths of exposed SWNTs could be varied on a device-by-device basis depending on the protein being investigated.

To date, we have investigated over 200 single-molecule devices using 13 different proteins and protein variants. Both optimization procedures described above have been used successfully. Once an attachment protocol has been developed for a particular protein, the yield of devices that produce single-molecule electronic signals is approximately 80%. Figure 3 shows two typical devices after they had been measured interacting with various solutions and protein substrates. With care and proper rinsing, the device surfaces remained clean enough to clearly image the SWNT and the attached biomolecules (arrows). Note that the typical SWNT diameter of 1 nm is much smaller than most proteins, so identifying attached protein in the images was straightforward. Comparable imaging is much more difficult to accomplish on rougher and larger metal films and nanowires.

## II. Measurement Techniques

Once an individual biomolecule has been attached to a SWNT device, the measurement protocol consists of recording electrical signals from the device. The protein motions do not by themselves generate voltage pulses, nor do the single-electron chemical events of binding or catalysis produce measurable current pulses. Instead, protein fluctuations affect the electrical resistance of the underlying SWNT conductor. Fortunately, SWNT resistance is acutely sensitive to local electrostatics, and a substantial proportion of a device's resistance can be concentrated at the position where a protein attachment most perturbs the SWNT channel. This co-location of attachment, resistance, and sensitivity combine to produce measurable electronic signals from a single protein.

To measure these changes in SWNT resistance, a constant bias of 50 to 100 mV is applied between the source and drain electrodes, causing a DC current of 1 to 100 nA to flow through the SWNT. Using a current preamplifier, this current and its fluctuations can be digitized, displayed to the user, and

stored for later analysis. Throughout Section III, example signals are plotted as current traces versus time $I(t)$. In cases where the DC component has been removed to accentuate the fluctuating portion, the relevant signal is $\Delta I(t)$ around a mean of zero. The temporal resolution of these signals is typically limited to the preamplifier's bandwidth. Without any device optimization and using only commercial instruments, resolutions of 10-50 μs are easily achieved, significantly faster than the shot-noise limitations of single molecule fluorescence techniques like FRET (27).

Most of our signal analysis has been performed using a 10-Hz, digital low pass filter to extract $\Delta I(t)$ from $I(t)$. However, semi-automated filtering like this must be performed with care because of two complications. First, SWNT devices have substantial background noise. The 1/f noise spectrum causes the "DC" current value to wander significantly during long duration measurements. This unpredictable wandering is very unlike the stable, background dark current in FRET, so it precludes the simple adoption of analysis techniques developed by that field over the past 20 years. Secondly, the SWNT technique allows individual molecules to be monitored for hours at a time. Many proteins exhibit dynamic disorder on time scales of seconds to minutes, and reliably distinguishing these signal components from underlying noise remains a signal processing challenge.

Finally, the electrical measurements are performed with the active portion of the SWNT device submerged in electrolyte solutions. Application of the fluid has been done using a micropipette, microfluidics, or a simple droplet technique. Whichever the case, the electrical potential of the fluid should be held constant with a low-noise voltage source. A single Pt wire in good contact with the electrolyte can serve as a sufficient counter electrode. However, SWNT device performance depends upon the electrolyte's potential, and selecting a potential that maximizes sensitivity is beneficial. For this purpose, an additional reference electrode and electrochemical potentiostat is usually necessary. An electrochemist's conventional 3-electrode configuration ensures reproducible measurement of the SWNT's gating characteristics and the most reliable electrolyte biasing (28).

When properly fabricated, these devices have excellent mechanical, thermal, and chemical stabilities. The measurement techniques described here allow an individual molecule to be monitored in liquids or gases over minutes, hours, or even days. Spontaneous device failure has not typically been a problem with proper handling and storage. At the longest durations, devices are susceptible to the same problems of biofouling faced by all bioelectronics.

## III. Three Examples of Single Molecule Enzymology

III-A. Lysozyme

Lysozyme is an innate enzyme of the mammalian immune system. It attacks the cell walls of gram-positive bacteria, resulting in cell lysis. The enzyme functions by catalyzing the hydrolysis of

glycosidic bonds in the peptidoglycan layer of bacterial cell walls. Various orthologs of lysozyme have been isolated from diverse sources, ranging from chicken eggs to the T4 bacteriophage.

Having been studied for over one century, much is known about lysozyme's structure and function. X-ray crystal structures show that lysozyme has two domains connected via a "hinge" domain, and that the enzyme opens and closes around this hinge when binding peptidoglycan (*29, 30*). Single-molecule FRET studies have observed this hinge motion dynamically during binding (*31*). However, careful observations also determined that successful catalysis does not always accompany mechanical hinge motion. When the hinge opens and closes at rates of $10 - 80$ s$^{-1}$, glycosidic bonds are being broken. Faster motions in a distinct range of $200 - 400$ s$^{-1}$ do not result in hydrolysis, even when peptidoglycan appears to be properly bound (*31-34*). Unexplained behaviors such as this, combined with a wealth of single-molecule FRET data, made lysozyme an excellent candidate for demonstrating the SWNT-based single molecule bioelectronics.

The lysozyme of bacteriophage T4 was synthesized, purified, and then attached to SWNT devices as described in Section I. To ensure reproducible attachment orientations from one device to another, we synthesized a single-cysteine, pseudo-wild-type variant (with the following mutations: C54T / C97A / S90C, hereafter referred to generically as "lysozyme"). Figure 1 schematically depicts the resulting device, with site S90C anchored to the SWNT sidewall and the hinge domain and peptidoglycan binding site freely accessible to the surrounding solution. Devices were then measured in phosphate buffered saline (PBS; 138 mM NaCl, 2.7 mM KCl, 8.1 mM Na$_2$HPO$_4$, 1.5 mM KH$_2$PO$_4$, pH 7.5) with and without peptidoglycan. Uninterrupted electrical monitoring was typically conducted for 600 s.

Figure 4 shows the three different types of electronic signals that composed all of the recordings. Approximately 5% of the time that peptidoglycan was present, $\Delta I(t)$ remained quiet without significant fluctuations outside the envelope of SWNT background noise (Fig. 4a). The remaining 95% of our recordings were filled with two-level fluctuations of positive current excursions $\Delta I(t)$ above a background level. When peptidoglycan was removed from the measurement solution, these excursions stopped completely and the device returned to its inactive, open conformation.

$\Delta I(t)$ excursions fell into two distinct categories shown in Figs. 4b and 4c. Approximately half the time, $I(t)$ fluctuated rapidly at a rate of 200 to 400 s$^{-1}$. During the remaining time, $I(t)$ fluctuated with the same magnitude but at slower rates of 15 to 60 s$^{-1}$. Single molecule FRET measurements have frequently reported similar observations, with lysozyme molecules in either the faster, nonproductive state or the slower, catalytically productive one (*31-34*). The 600-s duration of the SWNT measurements allowed direct observation of interconversions between the two behaviors. A molecule would stably process at the slower rate for 8 to 10 seconds, on average, before transitioning into the faster rate for a

similar time. The long duration spent in one state or the other indicated a very long-term memory effect that had not previously been well characterized.

To further evaluate the $\Delta I(t)$ fluctuations, histograms were built of the low ($\tau_{lo}$) and high ($\tau_{hi}$) durations spent during each individual excursion. Initially, histograms of raw data showed biexponential distributions for $\tau_{lo}$ and $\tau_{hi}$. Separating the fast- and slow-rate segments from each other, however, proved that the biexponential form was an artifact of lysozyme's two types of motion. Consequently, all of the fast-rate portions of a 600-s data set were combined together into one data subset, and the slow-rate portions were treated as a separate subset. Figure 5 shows example $\tau_{lo}$ and $\tau_{hi}$ distributions, color-coded to correspond to the two types of motion depicted in Fig. 4. All four distributions fit single mean time constants $<\tau_{lo}>$ or $<\tau_{hi}>$, with an average turnover rate $k_{cat}$ calculated as $k_{cat} = (<\tau_{lo}> + <\tau_{hi}>)^{-1}$ (35). During the slower, catalytically effective motions, $k_{cat} = 15.4$ s$^{-1}$. During the faster, catalytically nonproductive motions, $k_{cat} = 316$ s$^{-1}$.

Because of the stability of the electronic device architecture, individual molecules could be easily studied for long durations. For example, we observed enough interconversions between the fast- and slow-rate behaviors to define a mean duration $<\tau_{mem}>$ for the memory effect that causes the molecule to be in one state or the other. $<\tau_{mem}>$ was measured to be approximately 8 s for both the fast- and slow-rate behaviors. On average, the molecule spent 8 s processing peptidoglycan at the rate $k_{cat} = 15.4$ s$^{-1}$, and then the next 8 s opening and closing without catalysis at a rate $k_{cat} = 316$ s$^{-1}$.

Long duration measurements also allowed the activity of a single molecule to be measured under different conditions. Measurements were performed at pH 5, 7, and 11 to investigate how $\tau$, $k_{cat}$, and $<\tau_{mem}>$ each varied with pH. Table 1 summarizes this work, showing all of the parameters for each condition. Away from pH 7, the slow, processive motions slowed down by about 25% but $<\tau_{mem}>$ increased by a similar fraction, so that the processive activity was only minimally affected. On the other hand, the slow processing was interrupted by longer and more frequent inactive periods at pH 5 and 11. This shift caused the proportion of time spent in the catalytically-active state to drop, leading to 60-70% decreases in the effective processing rate.

Overall, nine independent parameters governing the lysozyme motion were directly measured from a single molecule as a function of pH. These included $<\tau_{lo}>$, $<\tau_{hi}>$, $<\tau_{mem}>$, and the total mean proportion of time spent in the fast-rate state, the same parameters for the slow-rate state, and $<\tau_{mem}>$ for the inactive state. This level of detail is unique to the electronic technique described here, and provides meaningful opportunities for comparison to the results of theoretical modeling.

A final element included in Table 1 is the relative energy difference $\Delta E$ between the molecule's open and closed conformations. Within Boltzman statistics, the ratio of $<\tau_{lo}>$ to $<\tau_{hi}>$ provided the

relative thermodynamic probability of being in one state versus the other as $\Delta E = k_B T \ln(<\tau_{hi}> / <\tau_{lo}>)$. During the fast, nonproductive motions, $\Delta E$ measured only 1.4 kcal/mol, equivalent to forming and breaking a salt bridge or hydrogen bond. When the nonproductive activity converted to the slower, catalytic processing, $\Delta E$ increased by 1.1 kcal/mol. This increase was interpreted as the additional energy required for the catalytic hydrolysis to occur, which must be matched by energy released during glycoside hydrolysis for this thermodynamically favorable process.

A single molecule measured on multiple days tended to produce similar $\tau$ distributions that could be added to each other to improve the reliability of the fitting. Different molecules, on the other hand, produced distributions with different mean values. Among eight different lysozyme molecules, $k_{cat}$ values ranged from 10 to 60 s$^{-1}$ with an average of 30 s$^{-1}$ for the slower motions. For the faster activity, $k_{cat}$ ranged from 120 to 600 s$^{-1}$ with an average of 280 s$^{-1}$. This molecule-to-molecule variation suggested static disorder with a longer time scale than the measurement duration. One source of such disorder could be the perturbing influence of the SWNT device, but native conformational disorder could also play a role. A promising direction for future experiments would be to denature and refold a single lysozyme molecule, to see whether the conformational energy landscape can be sampled more widely to better test the ergodic hypothesis using a single molecule.

Long duration single-molecule measurements provided thousands of independent events that enabled reliable event statistics to be calculated. A final metric of particular interest to the single molecule community is the normalized variance $r$, defined to be the variance divided by the mean value

$$r = \sigma^2 / <\tau>^2 = \sum_i \left(\tau_i - <\tau>\right)^2 / \sum_i \tau_i^2 . \qquad \text{Eqn. 1}$$

When a reaction involves only one rate-limiting step, then $r = 1$. When two or more rate-limiting steps occur in succession, then $r < 1$, with a limiting case of $r = 1/n$ when $n$ different rate-limiting steps have similar rate constants (36-38).

In lysozyme, $r_{open}$ was observed to have values of $1.0 \pm 0.1$, indicating that the waiting time for enzyme closure was determined by only one rate-limiting chemical step. On the other hand, $r_{closed}$ was always significantly less than unity. $r_{closed}$ measured $0.74 \pm 0.12$ during catalytic processing and $0.43 \pm 0.06$ during nonproductive motions, both of which indicated two or more rate-limiting steps in the reopening of the enzyme. Similar analysis at three pH values is summarized in Table 2, showing that the $r$ values remained relatively constant.

In a separate experiment, the peptidoglycan was synthesized without the peptide crosslinks that make it an effective, two-dimensional bacterial cell wall. To investigate the effect of the crosslinks on lysozyme's activity, individual lysozyme molecules were probed processing the synthetic, linear polymer

9

or natural, crosslinked peptidoglycan. The main difference was the nearly complete elimination of the fast-rate, nonproductive binding when crosslinks were absent.

Figure 6 depicts this result using data sequences that have been color-coded to distinguish the slow, fast, and inactive periods. Low magnification is used to emphasize the long-duration interconversion from one type of behavior to another. In addition, pie charts to the right of each graph summarize the average values of full data sets. The main effect of crosslinks is immediately visible in either representation of the data. When processing the linear polymer, the periods of fast, nonproductive motions (blue) are much shorter and less frequent, and the total time spent in such motions drops from 43% to only 7% of the total record. Average rates shown in the pie chart indicate that removal of crosslinks was also accompanied by 15 to 20% increases in $k_{cat}$ for both the fast- and slow-rate states.

Previous lysozyme studies had suggested that lysozyme was a processive enzyme, catalyzing many glycosidic bonds in succession before dissociation from the peptidoglycan substrate (*32*). In the absence of crosslinks, continuous catalytic activity was clearly observed for periods of 10 to 30 seconds without any inactive gaps caused by substrate release. These durations corresponded to the catalytic hydrolysis of many hundreds of glycosidic bonds, definitively confirming lysozyme as a processive enzyme. Furthermore, the role of the fast, nonproductive motions was clearly associated with the lysozyme encountering crosslinks as it processed along a peptidoglycan chain. Our current hypothesis is that the faster motions are associated with a mode of activity in which lysozyme transits from one strand to another, bypassing a crosslink. Substrate dissociation is not observed at the end of these nonproductive periods. In that case, $<\tau_{mem}>$ and its pH dependence can be interpreted as the mean time for such a transit to be successful.

In summary, the study of lysozyme with the SWNT FET technique provided a detailed look at single molecule activity and processivity. Aided by long duration, continuous recordings from an individual molecule, we avoided the ambiguities of molecule-to-molecule variation to directly measure kinetic variability, the different constituent components that contribute to ensemble catalytic rates, the role of peptidoglycan crosslinks, and lysozyme's response to those crosslinks.


III-B. DNA polymerase I

All living organisms depend upon DNA and require accurate DNA replication and repair mechanisms. DNA polymerases play the key role in DNA replication and repair. Many families of DNA polymerases exist, but they all share a common catalytic subdomain that slides along a single-stranded DNA template and sequentially incorporates complementary deoxyribonucleotide triphosphates (dNTPs) to form base pairs (*39, 40*). One depiction of the replication catalytic cycle is depicted in Figure 7 (*41*).

More specifically, DNA polymerases have multiple domains that are frequently labeled according to their similarity to a human right hand. The "thumb" domain binds to a DNA template, the "fingers" domain recognizes and binds the appropriate dNTP, and the two are brought together around a "palm" domain in which incorporation takes place. After a successful catalytic incorporation, the polymerase must translocate along the template strand as well as proofread the product base pair to minimize transcription errors. The simplest components of the catalytic cycle include the opening and closing of the fingers domain. This motion has been extensively studied by single molecule FRET techniques (*42, 43*), and it is depicted in Fig. 7 with shading to indicate uncertainties in the precise timing of the re-opening. In contrast to this main motion, the kinetics and mechanistic details of dNTP recognition and product proofreading remain poorly understood. New techniques are needed for probing the relationship between conformational states and intermediate steps in the catalytic cycle. Consequently, DNA polymerase is an ideal candidate for the single molecule bioelectronic technique described here.

Our work has focused on the Klenow fragment (KF) of DNA polymerase I, an enzyme that has been widely studied due to its simplicity in activity and expression. KF was synthesized, purified, and then attached to SWNT devices using the techniques described in Section I. As with lysozyme, we synthesized a particular KF variant (D355A / E357A / L790C / C907S, hereafter referred to as KF) that incorporated a single cysteine for SWNT attachment. Other point mutations deactivated the exonuclease domain that normally controls proofreading. The L790C site is located on the back side of the finger domain, so that after attachment the active domains extended away from the SWNT and $SiO_2$ surface, remaining free to bind template strands and dNTPs. Measurements were performed with the devices submerged in a standard buffered solution (10 mM Tris, 50 mM NaCl, 10 mM $MgCl_2$, 10 mM DTT, pH 7.8) using homopolymeric DNA template (100 nM) and an excess of either complementary or non-complementary dNTPs (10 μM). The DNA templates consisted of a M13 forward primers to which KF initially binds, annealed to a 42-base homopolymer poly$(dA)_{42}$, poly$(dT)_{42}$, poly$(dC)_{42}$, or poly$(dG)_{42}$.

Figure 8 depicts typical time traces $\Delta I(t)$ from a single-molecule KF device probed with poly$(dA)_{42}$ template. The baseline noise level was first characterized in the presence of DNA template but without dNTP (Fig. 8a), and then different dNTPs were added. Fig. 8b shows that $\Delta I(t)$ excursions appeared when complementary dTTPs were added, whereas Fig. 8c depicts the same template mixed with noncomplementary dGTP. Measurements on the same device were separated by extensive rinsing with buffer to eliminate spurious signals caused by cross contamination. As long as this protocol was followed, we were able to test single devices with all 16 different combinations of DNA template and dNTPs. We only observed $\Delta I(t)$ excursions when complementary Watson-Crick base pairings were possible.

As with lysozyme, analysis of the $I(t)$ records from KF proceeded by identifying and enumerating $\Delta I(t)$ excursions and then examining their timing and statistics. Figure 8d magnifies the record of Fig. 8b

11

to show two example excursions and definitions of the durations $\tau_{open}$ and $\tau_{closed}$. Distributions of $\tau_{open}$ and $\tau_{closed}$ from many thousands of events followed simple Poisson statistics with single time constants, as shown in Figs. 9a and 9b for two different Watson-Crick base pairings. Fortunately, KF did not exhibit the complex rate switching observed with lysozyme, so analysis of the KF distributions was more straightforward. Even so, testing 16 different nucleotide combinations was data intensive. Table 3 summarizes the mean $\tau$, $r$ and $k_{cat}$ values observed for the 4 complementary combinations that produced $\Delta I(t)$ excursions. The KF excursions had the opposite sign of lysozyme excursions, being decreases of current rather than increases. This difference, which results from differences in the surface charges of the two enzymes, is addressed in detail in Section IV. In any case, it was straightforward to measure devices with different concentrations of dNTP to definitively determine that the high-current state corresponded to the enzyme's open configuration.

To confirm that nucleotide incorporation was the cause of the $\Delta I(t)$ excursions, additional experiments were performed in exceedingly low template concentrations (below $K_d = 5$ nM). At 1 nM, the diffusion-limited waiting time for arrival of a template molecule was estimated to be 3 s, growing even larger at lower concentrations. In that regime, continuous recordings observed long inactive periods interrupted by the processing of a single template molecule. Figure 10a shows an example 5-s data segment that can be interpreted in this manner. The burst of $\Delta I(t)$ excursions beginning at t = 2.2 s corresponded to template arrival and the beginning of KF processing. In this example, 42 distinct peaks could be counted before product release at t = 3.2 s. Histograms built from many similar burst sequences are shown in Fig. 10b. The histogram is strongly peaked at 42, matching the length of the DNA template and suggesting that KF efficiently processes to the end of the template molecule with one $\Delta I(t)$ excursion per base. A few events showed fewer that 42 events, which can occur when KF falls off the template. Virtually none of the burst sequences extended beyond 42.

Consequently, we conclude that each individual $\Delta I(t)$ excursion corresponded to a single nucleotide incorporation event. The processivity of KF clearly extends to at least 42 bases, in agreement with other reported estimates (*44, 45*). Experiments using longer templates could probably determine the upper limit for KF's processivity, but that issue was not pursued here.

Instead, we focused on the interpretation of $\tau$ values in Table 3. Given that $\tau_{open} + \tau_{closed}$ corresponds to exactly one catalytic cycle, it was appropriate to assign their sum to $k_{cat}^{-1}$ and to interpret the durations in terms of the cycle's individual steps (Fig. 7). The duration $\tau_{open}$ is one hundred times larger than $\tau_{closed}$ and has a normalized variance $r_{open}=1$. Thus, a single rate-limiting step in the open configuration controls the kinetics of the entire catalytic cycle. Generally, this step is believed to be the recognition and binding of the correct nucleotide to form the ternary complex $E \cdot DNA_n \cdot dNTP$ (*42, 43*). Furthermore, $<\tau_{open}>$ was nearly twice as long for the formation of dA-dT base pairs than for dG-dC pair.

This observation supports previous KF measurements of two distinct replication rates for the different Watson-Crick base pairs (*45, 46*). In contrast, $<\tau_{closed}>$ did not depend on the particular dNTP being incorporated, suggesting that the chemical step following enzyme closure does not distinguish between nucleotides or involve any recognition. In our model, exonuclease proofreading has been disabled, which could substantially affect this result. Even without exonuclease activity, though, $r_{closed}<0.8$, indicating that at least two rate-limiting steps occur in the closed configuration. In other words, at least one additional state in the catalytic cycle occurs in addition to nucleotide incorporation while the fingers domain remains closed. This result leads us to assign the enzyme opening as shown in Fig. 7.

We note that the $\tau_{open}$ and $\tau_{closed}$ distributions in Fig. 9 overlapped and were too broad to identify a nucleotide based on the timing of a single excursion. In the bioelectronic architecture, however, every single excursion can be characterized by three parameters: $\tau_{open}$, $\tau_{closed}$ and an excursion amplitude $\Delta I$. Histograms of sample magnitudes are included in Figs. 9b and 9c to illustrate that they were more distinct and nucleotide-specific than either $\tau$ value. On average, a dTTP incorporation produced an excursion $\Delta I$=-6 nA, whereas a dGTP incorporation produced an excursion $\Delta I$=-2 nA, both measured relative to the open-enzyme configuration. These amplitude differences are believed to result from different degrees of KF closure. Taking advantage of all three independent parameters may be a successful strategy for distinguishing different bases in heteropolymeric DNA templates.

In summary, the single molecule bioelectronic interface proved quite useful for investigating KF catalytic activity. The measurement clearly observed individual nucleotide incorporations and demonstrated processivity of at least the 42-base template lengths. The rate-limiting step of the catalytic cycle was confirmed to occur in the enzyme's open configuration, and different kinetic rates were observed for the incorporation of bases forming different base pairs. Although the results only begin to illuminate KF's full catalytic cycle, they demonstrate some of the possibilities for fruitful continued investigation using the bioelectronic technique.

III-C. Protein Kinase A

As a third enzyme example, we considered cAMP-dependent protein kinase A (PKA). PKA serves critical regulatory functions by phosphorylating a wide range of other proteins and enzymes, turning their activity on and off (*47-49*). Its correct function is a prerequisite for cell signaling, transcription, and metabolism. Mechanistically, PKA is interesting because of its versatile active site, which can promiscuously bind a wide range of substrates. In addition to substrate binding, PKA also binds two cofactors, $Mg^{2+}$ and adenosine-5'-triphosphate (ATP). In the presence of both cofactors, PKA transfers the gamma phosphate of the ATP to the target substrate (*47, 50, 51*).

To test PKA activity using the single molecule bioelectronic technique, we synthesized the catalytic subunit with a cysteine mutation (T32C) introduced on the enzyme surface. As in the previous cases, this site was designed to minimize interference with PKA's binding sites or native activity. After attachment of PKA to the SWNT devices, electronic recordings were acquired with the device submerged in a standard buffer (100 mM MOPs, 9 mM $MgCl_2$, 100 μM TCEP, pH 7.2). Devices were monitored in the presence of ATP (2 mM), the synthetic peptide substrate Kemptide (100 μM), or mixtures of ATP and Kemptide.

Figure 11 shows typical recordings of the current fluctuations $\Delta I(t)$ from single-molecule PKA devices. In buffer, $\Delta I(t)$ exhibited the noise typical of SWNTS (Fig. 11a). Individual binding events were immediately visible when the devices were measured in the presence of either ATP (Fig. 11b) or Kemptide (Fig. 11c). In both cases, NMR measurements have shown that PKA only partially closes to an intermediate configuration (*52, 53*). Both binding partners must be present to achieve the fully-closed, catalytically active configuration. When both PKA and ATP were present in solution, the PKA device exhibited three-level switching shown in Fig. 11d. $\Delta I(t)$ directly recorded the two-step binding sequence that takes PKA from its initial, open configuration, through the intermediate configuration and to the closed state. The right side of Fig. 11 includes histograms of all four traces to represent the relative weights and positions of the different $I(t)$ sublevels.

Statistical analysis of each trace in Fig. 11 provided different details about PKA activity. For example, Fig. 11b depicts the bound and unbound durations for just the ATP site. The distributions of these durations then provide measurements of $k_{on}$ and $k_{off}$ for ATP. The details of these distributions are highlighted in Figure 12. A single exponential fit to each distribution determines the values of $\tau_{bound}$ and $\tau_{unbound}$ (Fig 12). However, in both cases the exponential fitting excludes longer-lived events in the tail of the distribution. Because of these long tails, the arithmetic mean durations $<t_{bound}>$ and $<t_{unbound}>$ are always longer than the corresponding $\tau_{bound}$ and $\tau_{unbound}$.

While the distinction between $<t>$ and $\tau$ might appear merely mathematical, it proves quite useful for understanding PKA's variability. In practice, the majority (>95%) of ATP binding events are described by the $\tau$ exponential fitting, and this portion of the distribution does not change from one second to another. On the other hand, the makeup of the distribution's tail changes appreciably second by second. This variation is represented in Fig. 12b by plotting the mean value $<t>$ calculated in 1-s increments. During one moment, a negligible number of events in the tail can cause $<t> \approx \tau$, at a different time, multiple long-lived events cause $<t>$ to increase to $10\tau$ or even $100\tau$. Fig. 12b illustrates a multi-second memory in which periods with longer or shorter tails tend to persist for many consecutive seconds or, in other words, through many thousands of ATP binding/unbinding cycles. This variability

14

and memory effect indicate the degree to which PKA conformational motions affect ATP binding, and indirectly highlight the potential for PKA regulation.

The situation is nearly identical for the substrate binding site. Figure 13 provides similar graphs for Kemptide binding and unbinding times and their second-by-second variations.

Table 4 shows the long-duration numerical averages for ATP and Kemptide binding, with error bars of one standard deviation $\sigma$ for each parameter. For all four $\tau$ values, temporal stability leads to very small $\sigma$ and maximum possible rates for the binding/unbinding cycle. However, the <t> values are more appropriate for comparison to ensemble data, since they include the whole range of possible events. Variability in <t> causes $\sigma$ to be relatively large and reduces the effective rate by 60-65%. The direct measurement of this variability is an enormous improvement to our understanding of PKA activity. Previously, ensemble measurements had only been able to estimate or put limits on the rates of these transient events (*54-56*).

Finally, we return to the complex $\Delta I(t)$ signal that occurs in the presence of both ATP and Kemptide. With both binding partners present, PKA can form the fully-closed, ternary complex that is catalytically active. Analysis of $\Delta I(t)$ recordings shown in Fig. 11d result in 3x3 matrices of transition probabilities and kinetic rates between each of the open, intermediate, and closed configurations. Here, we focus on just one aspect of these rates, namely the duration of one complete catalytic cycle.

Figure 14a highlights a short segment of $\Delta I(t)$ to illustrate the highly variable routes by which catalytic cycles were completed. The simplest possible trajectory involved three transitions, first from the open conformation to the intermediate one, then to the fully-closed conformation, and finally back to the open conformation with product release. A large number of trajectories followed this sequence, and one example is shown in Fig. 14a. However, in a minority of trajectories, enzyme closure was not followed by a complete opening but rather by the intermediate conformation and a second closure. Fig. 14b illustrates an extreme example in which 9 closures occurred before PKA opened. Successful phosphorylation always results in product release; so we interpret the multiple closures as resulting from repeated attempts at phosphorylation, possibly with mechanical reorientation of the substrate during each partial opening. Fig. 14c categorizes over 10,000 catalytic turnovers according to the number of closures observed in each. While almost 80% of the turnovers occur using the simplest possible trajectory (with a mean $k_{cat} = 155$ s$^{-1}$), at least 10% of events require 3 or more repeated closures ($k_{cat} = 37$ s$^{-1}$). These minority events have major implications for the molecule's average turnover rate, since they occur many times slower than the single-closure trajectory.

In summary, PKA is a highly variable enzyme, which befits its role regulating and being regulated in key biological processes. The single molecule bioelectronic device proved ideal for observing this variability, even under the simplest experimental conditions. The binding/unbinding cycle

of the ATP and substrate sites were investigated separately, and then the full catalytic cycle was observed with surprising observations of inefficient processing. The $\Delta I(t)$ recordings contained a level of detail that will be ideal for studying PKA's function in more complex environments, and that suggest enormous opportunities for investigating binding by inhibitors and other binding partners.

### IV. Transduction Mechanisms and Generalization to Other Biomolecules

The previous sections have focused on the types of data and data analysis that can be obtained using single molecule bioelectronics. We conclude with a discussion of the electrostatic mechanisms that make these device effective, and how those mechanisms can be tailored and controlled. Despite achieving success with three different enzymes, further generalization of the architecture will benefit from a thorough understanding of the transduction mechanisms at work in these devices.

First and foremost, SWNTs are highly sensitive conductors. Fluctuating point charges near a SWNT, such as from a charge trap in $SiO_2$ or the moving tip of a scanning probe microscope, have been demonstrated to strongly affect SWNT conductance via electrostatic gating (*57*). The main mechanism behind this sensitivity is not electrostatic doping *per se*, but is rather due to a potential barrier being introduced along the conduction pathway (*57*). In a higher-dimensional film or a high-carrier-density nanowire, electrostatic screening minimizes such barriers. SWNTs, though, are one-dimensional wires with very low carrier densities. Consequently, the potential from an external charge is not screened very effectively (*58, 59*), and it can modulate the entire current flowing along the SWNT.

This sensitivity is critical to good signal transduction, but it also leads to significant environmental noise and device-to-device variability. Clean fabrication procedures, passivation of the metal electrodes with protective layers, and device annealing are all useful steps for obtaining well-behaved SWNT devices. However, absolute conductance values and their sensitivity to gating biases $V_G$ are very difficult to control in an architecture with exposed elements. Thus, some degree of device-to-device uniqueness is unavoidable. Furthermore, it may not be possible to simultaneously eliminate noise and maximize transduction from single molecule attachments. Freely suspending SWNTs is one strategy for noise reduction (*60*), but it leads to less robust devices that are susceptible to mechanical failure during biofunctionalization or frequent exchanges of measurement environments. A second strategy of introducing point defects has been proven to enhance and concentrate SWNT sensitivity (*17, 19, 61*), but it also leads to losses of mechanical strength and chemical stability.

Fortunately, results to date show that these issues do not preclude productive single molecule research. As-fabricated devices have achieved reasonable signal-to-noise ratios without further optimization of background noise levels, and we have developed a robust, empirical method for dealing with device-to-device variability (*2, 4*). In fact, comparisons made across a range of SWNT devices have

helped to reveal their working mechanisms. Nominally identical lysozyme attachments have induced fluctuations of 20 nA in one device but just 2 nA in another, showing that $\Delta I$ is a very poor metric for comparing devices. Instead, device-to-device reproducibility depends upon measuring the characteristic curve gating dependence $I(V_G)$ of each device.

Each SWNT device has a characteristic curve $I(V_G)$ that is a macroscopic, ensemble measurement of that SWNT's conductance, local environment, and sensitivities. Semiconducting SWNTs can have steep $I(V_G)$ transitions due to the global depletion of free carriers, but metallic SWNTs also have $I(V_G)$ curvature due to the substrate and other non-homogeneities. Ultimately, an attached biomolecule acts like a contaminant, perturbing the three-terminal $I(V_G)$ characteristic with additional sensitivity concentrated at particular location. No two SWNT devices have identical $I(V_G)$ curves, so no two devices respond the same way to the motions of an attached protein. However, each protein does have an identical set of surface charges that undergoes identical motions upon binding and unbinding. The consequence of these motions is an effective change of gating conditions upon the SWNT. Essentially, the measured signal is

$$\Delta I = \frac{\partial I}{\partial V_G} \Delta V_G \propto \frac{\partial I}{\partial V_G} \sum_i q_i \left( \frac{1}{r_{i,1}} - \frac{1}{r_{i,2}} \right) \exp(-r_{i,1}/\lambda_D), \qquad \text{Eqn. 2}$$

where an effective dynamic gating $\Delta V_G$ arises from individual surface charges $q_i$ moving from one position to another, perhaps screened by a surrounding electrolyte with Debye length $\lambda_D$ (62). The slope $\partial I/\partial V_G$ is an empirical, device-dependent parameter, but otherwise Eqn. 2 does not have many free parameters. X-ray crystallography provides detailed knowledge of many protein's surface charges and positions.

Figure 15 illustrates the equivalence of describing a particular signal in terms of $\Delta I$ or $\Delta V_G$. For a particular two-level fluctuation, a histogram of the raw data can be fit to two populations with peaks separated by $\Delta I$. If those peaks are projected onto the device's $I(V_G)$ characteristic, one peak is associated with the operating point $V_G$=0 V. The second peak, which in this example is the smaller population at higher current, defines a new operating point shifted by the amount $\Delta V_G$. For the S90C lysozyme variant, all devices exhibited $\Delta V_G$=-0.19±0.02 V (2). More than 18 devices, having $\Delta I$ fluctuations of 3% up to 300%, gave consistent values for $\Delta V_G$, even when some devices used semiconducting SWNTs and other used metallic SWNTs. Furthermore, lysozyme, PKA and KF produced distinct $\Delta V_G$ values based on their particular charge distributions and allosteric motions.

To further investigate this effective gating, lysozyme measurements were performed using a range of NaCl concentrations. In Eqn. 2, the Debye length $\lambda_D$ should play a critical role screening protein charge motions when it is made short enough. Lysozyme was fluorescently assayed to be active in

concentrations ranging from 10 to 300 mM, so single molecule measurements were conducted in that range. Figure 16 shows that the signal amplitude indeed dropped as $\lambda_D$ decreased, with a maximum signal occurring around $\lambda_D$~1.0 nm. Fitting the data to a simple Debye model,

$$|\Delta I(\text{t})| = A/\text{x}_\text{o} \exp(-\text{x}_\text{o} / \lambda_D), \qquad\qquad \text{Eqn. 3}$$

provided a precise value for $x_\text{o}$, the relevant screening distance for the responsible charges. The fitting produced a value $x_o = 1.03 \pm 0.10$ nm, which is remarkably small given that lysozyme is 7 nm tall and that the binding site is 3.5 nm from the SWNT. The small $x_o$ indicated that catalysis at the far-away active site could not be directly sensed by the SWNT. Instead, allosteric motions of charges closer to the C90 attachment site must have been be responsible for the electrostatic gating.

Inspection of lysozyme's x-ray crystal structures indicated that only two amino acids were likely to be responsible for gating the SWNT (*29, 30*). Sites K83 and R119 were both positively charged acids within ~$x_o$ of the SWNT attachment site. Furthermore, they were the only two residues to move appreciably (~0.15 nm) during enzyme closure (*30, 63*). The two charges both move away from the SWNT upon closure, which is consistent with the negative $\Delta V_G$ observed experimentally.

To test the hypothesis that signal transduction was primarily due to these two residues, we performed site-specific lysozyme mutagenesis. The two target sites were individually varied into charge-neutral alanines (K83A and R119A) or negatively-charged glutamic acids (K83E and R119E). Seven lysozyme variants were synthesized and purified with net charges at positions 83 and 119 spanning from $N = \Sigma q_i/e = +2$ to -2. For example, the R119A and K83E/R119E variants had $N = +1$ and $N = -2$, respectively. Each variant was then attached to SWNT devices and monitored under identical conditions hydrolyzing peptidoglycan. The experiments included over 30 active SWNT devices.

In the presence of substrate, all devices exhibited the usual, dynamic two-level fluctuations $\Delta I(t)$. The effective gating $\Delta V_G$ for each device was then calculated as described above, and devices with the same variant were averaged. Figure 17 summarizes the results by plotting the average $\Delta V_G$ with $\pm 1\sigma$ error bars for each variant. Overall, the sign and magnitude of $\Delta V_G$ exactly match predictions of a simple electrostatic model, with $\Delta V_G$=-91$N$-34 mV. The presence of a single charged amino acid (at either site) produced an effective gating of 91 mV, and the combined effect of two charged amino acids was approximately twice as large. The charge neutral variant K83A/R119A produced the smallest fluctuations and an effective gating of only $\Delta V_G$=-34 mV. This variant was of particular interest because the signal was presumably generated by the combined effects of all other lysozyme surface charges or dipole moments. Although the distal domain had a net charge of +3 and a substantial hinge motion relative to C90, the effect of its motion was barely 1/3 as large as that from one charge at either site 83 or

119.  A more precise analysis of the electrostatics, including locations and motions of each amino acid, was reported in Ref. (*4*).

In principle, these findings can be used as "design rules" to successfully link any protein of interest to SWNTs and generate single molecule recordings.  Firstly, an attachment protocol must be chosen.  In this work, proteins were modified to have only one cysteine exposed on their outer surfaces.  The cysteine-maleimide linkage then proved to be quite reliable for attaching proteins to SWNTs.  Other attachment methods might be preferable for proteins containing multiple cysteines.  Second, the location of this cysteine (or other attachment site) on the protein must be chosen carefully.  One of our surprising findings was that the cysteine did not need to be close to the substrate binding site or the catalytically active site.  Actually, SWNT attachments at those positions could potentially interfere with the protein's native activity.  Instead, effective attachments sites can be far from those sites.

Finally, the most consequential aspect of the protein attachment is in selecting a site that will produce dynamic electrostatic effects upon the SWNT FET.  We found that the motions of a single amino acid were sufficient to generate strong dynamic signals, as long as that amino acid was located close to the SWNT attachment.  Typical Debye lengths are on the order of only 1 nm in relevant physiological buffers, so the SWNT was well shielded from more distant surface charges.  Within one Debye length, some amino acids will be uncharged and others will not move substantially.  Among the moving residues, coordinated motions will produce additive electrostatic effects.  In the case of lysozyme, two positive residues moved in concert to produce a strong signal that could be used to compare many similar SWNT devices.

## V.  Conclusion

Single molecule bioelectronics are proven here to be immediately achievable.  The techniques used to fabricate working devices did not require precise, high resolution lithography nor other nonstandard techniques.  The fabrication procedures were easily scalable, and the production of many devices in parallel is completely feasible.  The general physics of device operation have become well understood, to the point that new protein attachments can now be designed and implemented without long development times.  The device stability provides a breakthrough for single molecule techniques, since a molecule can be monitored indefinitely with microsecond temporal resolution.

Furthermore, the scientific opportunities for single molecule bioelectronics are shown here to be very exciting and impactful.  Initial experiments with the devices revealed new information about three different enzymes, two of which had already been extensively studied by single molecule FRET.  The results show that bioelectronic and FRET techniques are complementary, providing two independent probes for understanding a single molecule's motions and chemical activity.  In cases where fluorescent

labeling is not possible or undesirable, the bioelectronic technique is uniquely able to generate detailed recordings of single molecule activity. The ability to monitor protein binding or enzymatic activity in the presence of multiple cofactors, or under the influence of a particular mutation, promises to grow into a powerful tool for biological sciences and pharmaceutical development.

**References**

1. R. Roy, S. Hohng, T. Ha, *Nat. Methods* **5**, 507 (2008).
2. Y. Choi, I. S. Moody, P. C. Sims, S. R. Hunt, B. L. Corso, G. A. Weiss, P. G. Collins, *Science* **335**, 319 (2012).
3. Y. Choi, I. S. Moody, P. C. Sims, S. R. Hunt, B. L. Corso, D. E. Seitz, L. C. Blaszcazk, P. G. Collins, G. A. Weiss, *J. of the Am. Chem. Soc.* **134**, 2032 (2012).
4. Y. Choi, T. J. Olsen, P. C. Sims, I. S. Moody, B. L. Corso, M. N. Dang, G. A. Weiss, P. G. Collins, *Nano Lett.* **13**, 625 (2013).
5. P. C. Sims, I. S. Moody, Y. Choi, C. Dong, M. Iftikhar, B. L. Corso, O. T. Gul, P. G. Collins, G. A. Weiss, *J. Am. Chem. Soc.*, in press (2013).
6. T. J. Olsen, Y. Choi, P. C. Sims, O. T. Gul, B. L. Corso, C. Dong, W. A. Brown, P. G. Collins, G. A. Weiss, *J. Am. Chem. Soc.*, in press (2013).
7. G. Gruner, *Analytical and Bioanalytical Chemistry* **384**, 322 (2006).
8. A. Star, J. C. P. Gabriel, K. Bradley, G. Gruner, *Nano Lett.* **3**, 459 (2003).
9. A. Star, V. Joshi, T. R. Han, M. V. P. Altoe, G. Gruner, J. F. Stoddart, *Organic Letters* **6**, 2089 (2004).
10. K. Besteman, J. O. Lee, F. G. M. Wiertz, H. A. Heering, C. Dekker, *Nano Lett.* **3**, 727 (2003).
11. H.-M. So, K. Won, Y. H. Kim, B.-K. Kim, B. H. Ryu, P. S. Na, H. Kim, J.-O. Lee, *J. Am. Chem. Soc.* **127**, 11906 (2005).
12. M. S. Purewal, B. H. Hong, A. Ravi, B. Chandra, J. Hone, P. Kim, *Phys. Rev. Lett.* **98**, 186808 (2007).
13. P. G. Collins, in *Oxford Handbook of Nanoscience and Technology: Frontiers and Advances* A. V. Narlikar, Y. Y. Fu, Eds. (Oxford Univ. Press, Oxford, 2010).

14. E. Joselevich, H. Dai, J. Liu, K. Hata, A. H. Windle, in *Carbon Nanotubes* A. Jorio, G. Dresselhaus, M. S. Dresselhaus, Eds. (Springer-Verlag, Berlin, 2008), vol. 111, pp. 101-164.

15. L. An, J. M. Owens, L. E. McNeil, J. Liu, *J. Am. Chem. Soc.* **124**, 13688 (2002).

16. M. J. Biercuk, S. Ilani, C. M. Marcus, P. L. McEuen, in *Carbon Nanotubes* A. Jorio, G. Dresselhaus, M. S. Dresselhaus, Eds. (Springer-Verlag, Berlin, 2008), vol. 111, pp. 455-493.

17. B. R. Goldsmith, J. G. Coroneus, V. R. Khalap, A. A. Kane, G. A. Weiss, P. G. Collins, *Science* **315**, 77 (2007).

18. J. G. Coroneus, B. R. Goldsmith, J. A. Lamboy, A. A. Kane, P. G. Collins, G. A. Weiss, *ChemPhysChem* **9**, 1053 (2008).

19. B. R. Goldsmith, J. G. Coroneus, A. A. Kane, G. A. Weiss, P. G. Collins, *Nano Lett.* **8**, 189 (2008).

20. B. R. Goldsmith, J. G. Coroneus, J. Lamboy, G. A. Weiss, P. G. Collins, *J. Mat. Res.* **23**, 1197 (2008).

21. S. Sorgenfrei, C.-y. Chiu, R. L. Gonzalez, Y.-J. Yu, P. Kim, C. Nuckolls, K. L. Shepard, *Nat. Nanotechnol.* **6**, 126 (2011).

22. S. Sorgenfrei, C.-y. Chiu, M. Johnston, C. Nuckolls, K. L. Shepard, *Nano Lett.* **11**, 3739 (2011).

23. L. Prisbrey, G. Schneider, E. Minot, *J. Phys. Chem. B* **114**, 3330 (2010).

24. G. T. Hermanson, *Bioconjugate Techniques* (Academic Press, Inc., Chicago, ed. 2nd, 2008), pp.

25. R. J. Chen, Y. G. Zhan, D. W. Wang, H. J. Dai, *J. Am. Chem. Soc.* **123**, 3838 (2001).

26. C. Li, M. Curreli, H. Lin, B. Lei, F. N. Ishikawa, R. Datar, R. J. Cote, M. E. Thompson, C. Zhou, *J. Am. Chem. Soc.* **127**, 12484 (2005).

27. S. Johnson, S. Cain, *Appl. Optics* **47**, 5147 (2008).

28. A. J. Bard, L. R. Faulkner, *Electrochemical methods: fundamentals and applications* (Wiley, New York, ed. 2nd, 2001), pp. 833.

29. R. Kuroki, L. H. Weaver, B. W. Matthews, *Nat. Struct. Biol.* **2**, 1007 (1995).

30. R. Kuroki, L. H. Weaver, B. W. Matthews, *Science* **262**, 2030 (1993).

31. Y. Chen, D. H. Hu, E. R. Vorpagel, H. P. Lu, *J. Phys. Chem. B* **107**, 7947 (2003).

32. D. Hu, H. P. Lu, *Biophys. J.* **87**, 656 (2004).

33. H. P. Lu, *Current Pharmaceutical Biotechnology* **5**, 261 (2004).

34. Y. Wang, H. P. Lu, *J. Phys. Chem. B* **114**, 6669 (2010).

35. S. N. Xie, *Single Molecules* **2**, 229 (2001).

36. K. Svoboda, P. P. Mitra, S. M. Block, *Proc. Natl. Acad. Sci. U.S.A.* **91**, 11782 (1994).

37. M. J. Schnitzer, S. M. Block, *Cold Spring Harbor Symposia on Quantitative Biology* **60**, 793 (1995).

38.    W. L. Xu, J. S. Kong, P. Chen, *Journal of Physical Chemistry C* **113**, 2393 (2009).

39.    T. A. Steitz, *Journal of Biological Chemistry* **274**, 17395 (1999).

40.    E. Delagoutte, *Frontiers in Bioscience-Landmark* **17**, 509 (2012).

41.    C. M. Joyce, *Biochimica Et Biophysica Acta-Proteins and Proteomics* **1804**, 1032 (2010).

42.    Y. Santoso, C. M. Joyce, O. Potapova, L. Le Reste, J. Hohlbein, J. P. Torella, N. D. F. Grindley, A. N. Kapanidis, *Proc. Natl. Acad. Sci. U.S.A.* **107**, 715 (2010).

43.    S. Y. Berezhna, J. P. Gill, R. Lamichhane, D. P. Millar, *J. Am. Chem. Soc.* **134**, 11261 (2012).

44.    F. R. Bryant, K. A. Johnson, S. J. Benkovic, *Biochemistry* **22**, 3537 (1983).

45.    N. Kaushik, V. N. Pandey, M. J. Modak, *Biochemistry* **35**, 7256 (1996).

46.    C. M. Joyce, O. Potapova, A. M. DeLucia, X. Huang, V. P. Basu, N. D. F. Grindley, *Biochemistry* **47**, 6103 (2008).

47.    J. A. Adams, *Chemical Reviews* **101**, 2271 (2001).

48.    G. Manning, D. B. Whyte, R. Martinez, T. Hunter, S. Sudarsanam, *Science* **298**, 1912 (2002).

49.    S. S. Taylor, J. Yang, J. Wu, N. M. Haste, E. Radzio-Andzelm, G. Anand, *Biochimica Et Biophysica Acta-Proteins and Proteomics* **1697**, 259 (2004).

50.    B. E. Kemp, D. J. Graves, E. Benjamini, E. G. Krebs, *J Biol Chem* **252**, 4888 (1977).

51.    J. A. Adams, S. S. Taylor, *Biochemistry* **31**, 8516 (1992).

52.    Madhusudan, E. A. Trafny, N. H. Xuong, J. A. Adams, L. F. Teneyck, S. S. Taylor, J. M. Sowadski, *Protein Science* **3**, 176 (1994).

53.    N. Narayana, S. Cox, X. Nguyen-huu, L. F. Ten Eyck, S. S. Taylor, *Structure* **5**, 921 (1997).

54.    L. R. Masterson, A. Mascioni, N. J. Traaseth, S. S. Taylor, G. Veglia, *Proc. Natl. Acad. Sci. U.S.A.* **105**, 506 (2008).

55.    D. Q. Ni, J. Shaffer, J. A. Adams, *Protein Science* **9**, 1818 (2000).

56.    B. D. Grant, J. A. Adams, *Biochemistry* **35**, 2022 (1996).

57.    S. R. Hunt, D. Wan, V. R. Khalap, B. L. Corso, P. G. Collins, *Nano Lett.* **11**, 1055 (2011).

58.    F. Leonard, J. Tersoff, *Phys. Rev. Lett.* **83**, 5174 (1999).

59.    F. Leonard, A. A. Talin, *Nat. Nanotechnol.* **6**, 773 (2011).

60.    Y. M. Lin, J. C. Tsang, M. Freitag, P. Avouris, *Nanotechnology* **18**, 295202 (2007).

61.    B. R. Goldsmith, J. J. Mitala, J. Josue, A. Castro, M. B. Lerner, T. H. Bayburt, S. M. Khamis, R. A. Jones, J. G. Brand, S. G. Sligar, C. W. Luetje, A. Gelperin, P. A. Rhodes, B. M. Discher, A. T. C. Johnson, *ACS Nano* **5**, 5408 (2011).

62.    J. N. Israelachvili, *Intermolecular and surface forces* (Academic Press, London, 1991), pp.

63.    R. Kuroki, L. H. Weaver, B. W. Matthews, *Proc. Natl. Acad. Sci. U.S.A.* **96**, 8949 (1999).

**Figure Captions**

**Figure 1. Schematic cartoon of a single molecule electronic device.** A SWNT conductor, electrically connected at both ends, was biofunctionalized with a single enzyme molecule. Interactions between that molecule and its surrounding environment, depicted here as a T4 lysozyme and its substrate peptidoglycan, generate electrical signals in the underlying SWNT.

**Figure 2. Biofunctionalization scheme.** Pyrene-maleimide linker molecules adhered to the SWNT and provided reactive sites for protein attachment. In this scheme, any protein having a surface-exposed cysteine residue can be covalently linked to the maleimide.

**Figure 3. Ambient AFM topography images of example devices.** (a) A 1.5-nm diameter SWNT and a single molecule attachment of T4 lysozyme. The SWNT extended under a protective polymer layer (top and bottom stripes) to connect to source and drain electrodes. Note the low levels of nonspecific adsorption on the surface, which aided clear AFM imaging. (b) Another device at higher magnification, showing a SWNT before (inset) and after biofunctionalization.

**Figure 4. Example electronic signals from lysozyme-conjugated devices measured with peptidoglycan substrate.** (a) Inactive periods, accounting for about 5% of the recordings, had baseline $I(t)$ levels and fluctuations. (b) Rapid $\Delta I(t)$ excursions occurred when lysozyme bound peptidoglycan nonproductively. (c) Slower $\Delta I(t)$ excursions exhibited the mean rates for lysozyme's catalytic hydrolysis of peptidoglycan. Each closure of the lysozyme domain generated one upward excursion in $\Delta I(t)$.

**Figure 5. Histograms of $\Delta I$ excursion durations during lysozyme activity.** (a) Data from rapid, nonproductive binding fit a simple Poisson distribution with single time constants for both the closed, high-$I(t)$ conformation and the open, low-$I(t)$ conformation. (b) Data from the slower, catalytic activity had similar distributions with slower time constants. Numerical fitting results are tabulated in Table 1.

**Figure 6. Comparison of lysozyme activity (a) with and (b) without crosslinks in the peptidoglycan substrate.** Catalytic processing (green) in the recordings increases from 51% to 88% when crosslinks are absent. Additional numbers in parentheses indicate the average turnover rates for enzyme motions in either case. The nonproductive and catalytic processing rates both decrease when crosslinks are present. Color coding of the data matches Figs. 4 and 5, with an additional yellow color to highlight rare events when lysozyme became stuck in its closed conformation for unusually long periods.

**Figure 7. Minimal reaction pathway of KF.** Each key step in KF's catalytic polymerization of DNA template is shown with its accompanying mechanical motions. Hatched sections indicate uncertain alignments between chemical steps and mechanical movements.

**Figure 8. Example electronic signals from KF-conjugated devices.** $\Delta I(t)$ was recorded for KF binding poly(dA)$_{42}$ (a) in the absence of any dNTPs, (b) with complementary dTTPs, and (c) with non-complementary dGTPs. Brief $\Delta I(t)$ excursions below -4 nA are only observed when complementary base pair formation was possible. (d) At higher magnification, the timing and amplitude of individual excursions was enumerated for statistical analysis.

**Figure 9. Histograms of $\Delta I$ excursion durations and amplitudes during KF activity.** (a) KF closed duration, KF open duration, and $\Delta I$ histogram as measured with poly(dA)$_{42}$ template in the presence of dTTP. The $\Delta I$ histogram clarifies the full distribution of $\Delta I(t)$ excursion heights observed over long periods. (b) Distributions from the same KF molecule processing poly(dC)$_{42}$ template in the presence of dGTP. Compared to the A-T base pairing, the C-G base pairing had a 40% shorter $<\tau_{open}>$ and a 50% smaller $<\Delta I(t)>$. Numerical fitting results for all four complementary combinations are tabulated in Table 3.

**Figure 10. KF processing of a single template molecule.** (a) At template concentrations of 1 nM and below, bursts of many $\Delta I$ excursions were separated by multi-second, inactive pauses. The pause durations equaled the diffusional waiting time for template arrival. Under these conditions, the number of excursions (i.e. dNTP incorporations) could be counted and unambiguously associated with a single template molecule. (b) Histogram of the number of excursions per burst observed while processing poly(dC)$_{42}$ template. The peak at 42 bases matches the template length, indicating events where KF processed one entire template strand. Occurrences of less than 42 bases indicate template dissociation.

**Figure 11. Example electronic signals from PKA-conjugated devices.** (a) The PKA device measured in buffer defines a baseline current associated with the enzyme's fully open configuration. (b-d) $\Delta I(t)$ relative to the baseline measured in the presence of (b) 2 mM ATP, (c) 100 µM Kemptide, and (d) both ATP and Kemptide. $\Delta I(t)$ excursions to -10 nA and -20 nA correspond to the intermediate and fully closed conformations, respectively. $\Delta I(t)$ histograms shown to the right clearly indicate the different states in each case.

**Figure 12. Dynamic disorder of PKA with ATP.** (a) Histogram of $\Delta I$ excursion durations resulting from PKA-ATP binding and unbinding events. Exponential fits to each distribution determining the values $\tau_{bound}$ and $\tau_{unbound}$. (b) Average durations $<t_{bound}>$ and $<t_{unbound}>$ calculated in 1 s bins, indicating the variable nature of ATP binding and unbinding rates. The average duration infrequently decreased to the corresponding $\tau$ value, which are depicted as dashed lines. These convergences indicate moments when the entire distribution was well-fit by a simple exponential without a long-duration tail.

**Figure 13. Dynamic disorder of PKA with Kemptide.** (a) Histogram of $\Delta I$ excursion durations resulting from PKA-Kemptide binding and unbinding events. (b) As with ATP, Kemptide binding and unbinding rates varied from one second to the next, though in the case of Kemptide an anticorrelation of the two rates was observed.

**Figure 14. Efficiency of PKA activity.** (a) An example $I(t)$ segment representing the simplest catalytic cycle, in which the open enzyme closed once and then fully opened, with a brief pause at the intermediate conformation. (b) A more "inefficient" cycle, with 9 repeated closures from the intermediate conformation before PKA finally returned to its open state. (c) Probability distribution of >10,000 re-opening events. Approximately 77% of all re-openings occurred after a single closure, but 5% of re-openings did not occur until after four or more repeated closures. The probability of an event such as the one in (b) was about 0.2%.

**Figure 15. Conversion of $\Delta I$ into an effective gating $\Delta V_G$.** (a) An example $I(t)$ trace for lysozyme processing peptidoglycan. (b) A histogram of $I(t)$ can be fit to two peaks corresponding to the open and closed conformations. (c) $I(V_G)$ curve for the same device, obtained using electrolyte gating. The major peak of the histrogram aligns with $I(V_G=0)$, the operating point of the device. The minor peak of the closed configuration is higher in current by $\Delta I$, which is equivalent to an effective gating of $\Delta V_G$.

**Figure 16. Debye screening of signal strength.** A single lysozyme molecule measured in various salt concentrations produced $\Delta I$ excursions of different magnitudes. The solid line is a fit to Eqn. 3 for Debye screening.

**Figure 17. Average transduction by seven T4 lysozyme variants.** (top) Lysozyme residues 83 and 119 were mutated away from their native, positive sidechains (blue) to be either neutral (yellow), or negative (red) as depicted. (bottom) The effective gating $\Delta V_G$ produced by each variant varied from 116

to -205 mV, with a value of -34 mV for the neutral $N = 0$ variant.  Error bars indicate three standard deviations as determined from up to 10 different devices fabricated with each particular variant.

| | Parameter | pH 5 | pH 7 | pH 11 |
|---|---|---|---|---|
| **Catalytic Processing (slow rate)** | $<\tau_{hi}>$ (ms) | 0.76 ± 0.05 | 0.95 ± 0.08 | 0.78 ± 0.09 |
| | $<\tau_{lo}>$ (ms) | 87 ± 3.0 | 64 ± 2.0 | 86 ± 3.0 |
| | $\Delta E$ (kcal/mol) | 2.84 | 2.53 | 2.82 |
| | $k_{cat}$ (s$^{-1}$) | 11.4 | 15.4 | 11.5 |
| | $<\tau_{mem}>$ (s) | 9.3 ± 5.1 | 8.0 ± 3.0 | 12.0 ± 4.4 |
| | % time in state | 16.3% | 41.1% | 21.1% |
| | time-averaged catalytic rate (s$^{-1}$) | 1.8 | 6.3 | 2.4 |
| **Nonproductive Binding (fast rate)** | $<\tau_{hi}>$ (ms) | 0.25 ± 0.01 | 0.26 ± 0.01 | 0.36 ± 0.01 |
| | $<\tau_{lo}>$ (ms) | 4.80 ± 0.35 | 2.90 ± 0.10 | 3.90 ± 0.17 |
| | $\Delta E$ (kcal/mol) | 1.77 | 1.45 | 1.43 |
| | $k_{cat}$ (s$^{-1}$) | 198 | 316 | 235 |
| | $<\tau_{mem}>$ (s) | 6.2 ± 4.0 | 7.9 ± 2.3 | 5.4 ± 1.8 |
| | % time in state | 72.4% | 52.1% | 63.8% |
| **Inactive** | $<\tau_{mem}>$ (s) | 0.83 ± 0.63 | 0.72 ± 0.25 | 0.96 ± 0.53 |
| | % time in state | 11.3% | 6.8% | 15.0% |

**Table 1.** Single molecule kinetic parameters for lysozyme processing peptidoglycan substrate.

| | Parameter | pH 5 | pH 7 | pH 11 |
|---|---|---|---|---|
| **Catalytic Processing (slow rate)** | $r_{closed}$ | 0.68 ± 0.15 | 0.74 ± 0.12 | 0.60 ± 0.15 |
| | $r_{open}$ | 1.00 ± 0.18 | 1.06 ± 0.15 | 1.11 ± 0.23 |
| **Nonproductive Binding (fast rate)** | $r_{closed}$ | 0.48 ± 0.10 | 0.43 ± 0.06 | 0.61 ± 0.08 |
| | $r_{open}$ | 0.97 ± 0.13 | 0.99 ± 0.09 | 1.00 ± 0.10 |

**Table 2.** Normalized variances of lysozyme rates.

| Template: | poly(dT)$_{42}$ | poly(dA)$_{42}$ | poly(dG)$_{42}$ | poly(dC)$_{42}$ |
|---|---|---|---|---|
| Nucleotide: | dATP | dTTP | dCTP | dGTP |
| $\tau_{\text{closed}}$ (ms) | $0.33 \pm 0.08$ | $0.42 \pm 0.09$ | $0.32 \pm 0.07$ | $0.33 \pm 0.05$ |
| $r_{\text{closed}}$ | $0.85 \pm 0.09$ | $0.83 \pm 0.06$ | $0.78 \pm 0.05$ | $0.78 \pm 0.05$ |
| $\tau_{\text{open}}$ (ms) | $71.4 \pm 1.4$ | $63.7 \pm 1.1$ | $39.0 \pm 5.6$ | $38.0 \pm 5.8$ |
| $r_{\text{open}}$ | $0.95 \pm 0.08$ | $0.96 \pm 0.06$ | $0.98 \pm 0.06$ | $1.03 \pm 0.07$ |
| $k_{\text{cat}}$ (s$^{-1}$) | $14.4 \pm 2.9$ | $16.0 \pm 2.9$ | $26.2 \pm 4.4$ | $28.5 \pm 3.5$ |
| $\Delta I$ (nA) | 6.94 | 4.9 | 2.53 | 2.4 |

**Table 3.** Single molecule kinetic parameters for KF processing homopolymeric templates.

| | **Single-Molecule** | | **Ensemble** |
|---|---|---|---|
| **ATP** | $\tau$ | $< t >$ | $< t >$ |
| bound (ms) | $1.99 \pm 0.03$ | $3.1 \pm 4.3$ | 5.3 (*55*) |
| unbound (ms) | $0.77 \pm 0.01$ | $5.0 \pm 19$ | $> 0.25$a |
| binding/unbinding cycle (s$^{-1}$) | $362 \pm 5$ | 125 | $< 190$ |
| **Kemptide** | $\tau$ | $< t >$ | $< t >$ |
| bound (ms) | $0.77 \pm 0.01$ | $1.8 \pm 2.9$ | <2 (*56*) |
| unbound (ms) | $0.67 \pm 0.01$ | $1.7 \pm 3.7$ | <20 (*54*) |
| binding/unbinding cycle (s$^{-1}$) | $696 \pm 8$ | 286 | >46 |

[a]Estimated by extrapolation to saturation conditions from the experimental data of Ni et al. (*55*)

**Table 4.** Single molecule kinetic parameters for PKA binding to ATP or Kemptide.

Figure 1



SWNT

Pyrene-maleimide

π−π
Stacking

Protein(Cys)

Thioether
Bond

**Protein**

Figure 2



a)
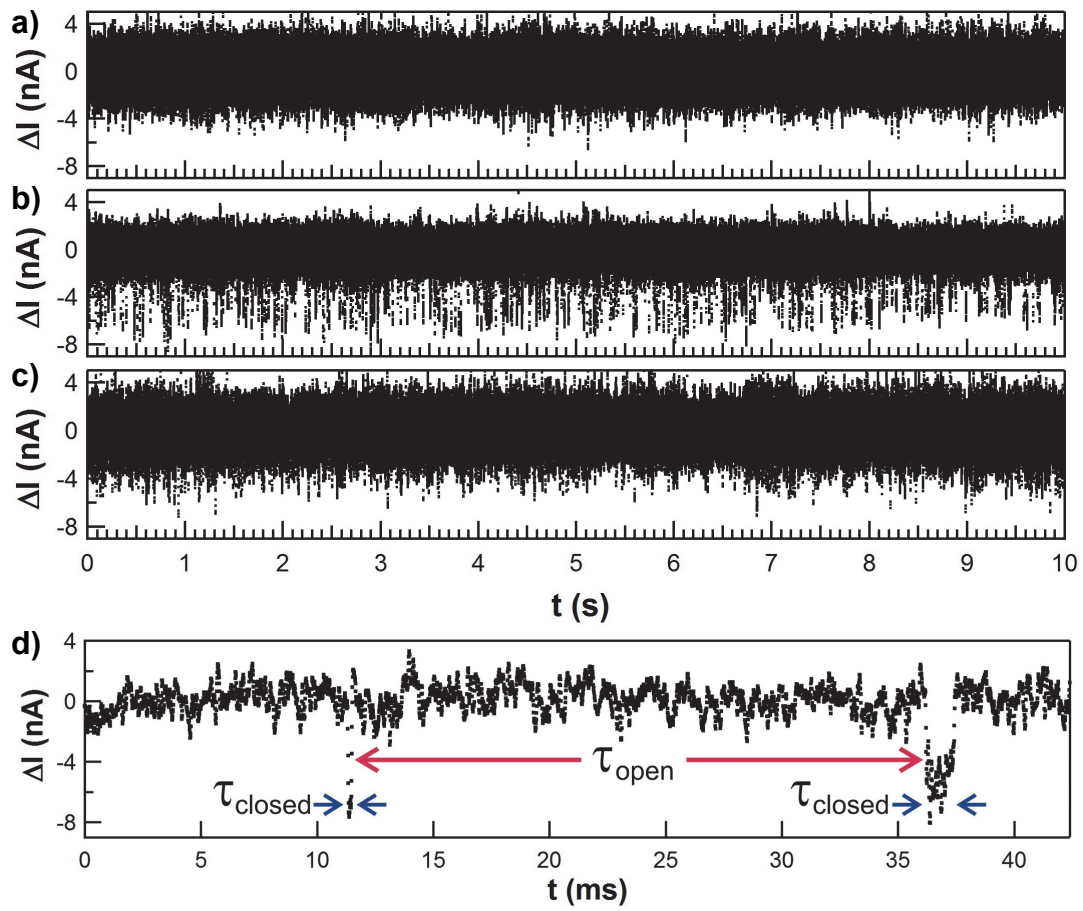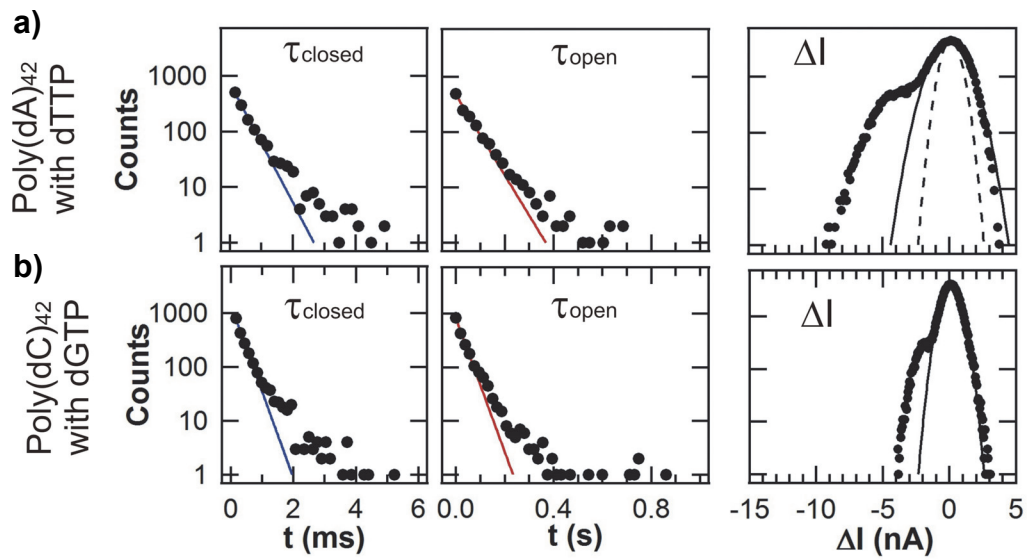
1 μm

b)

0.2 μm
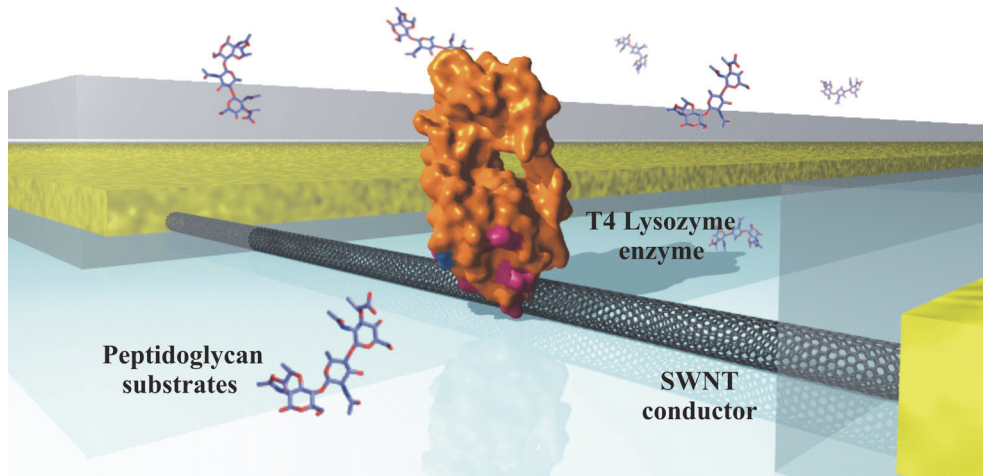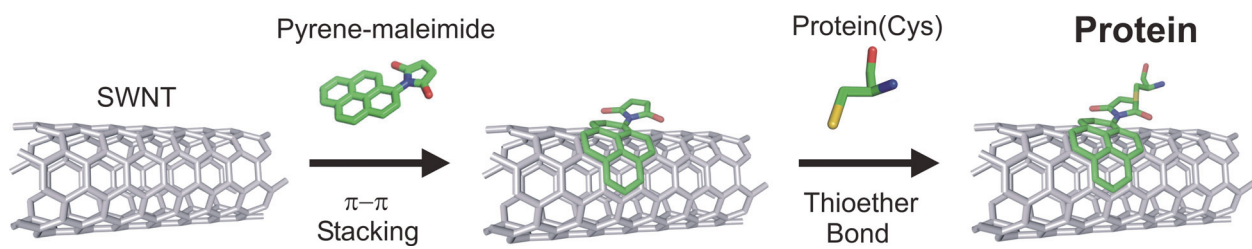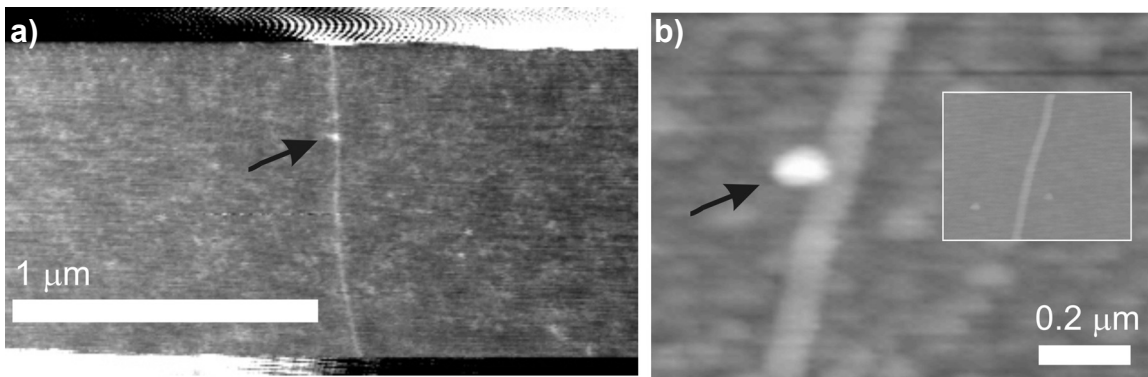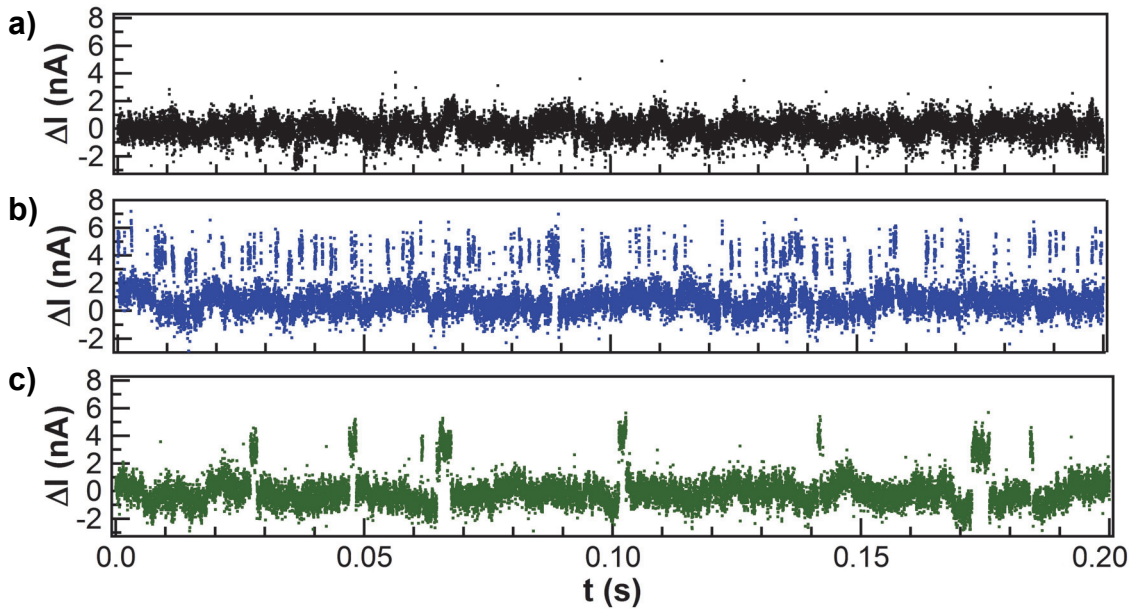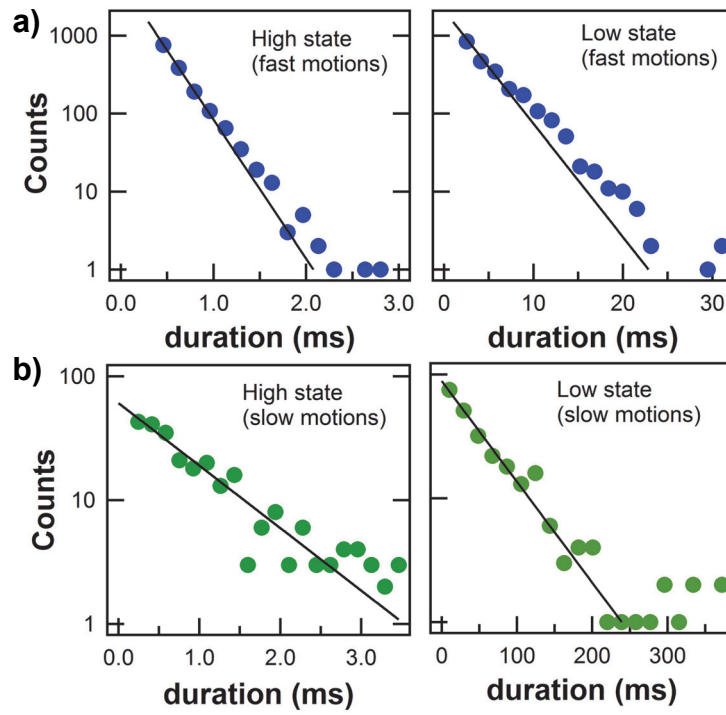
Figure 3

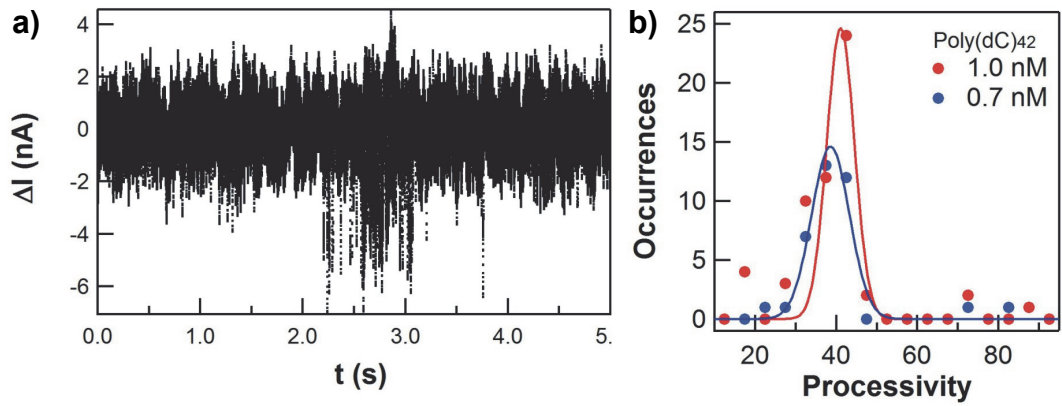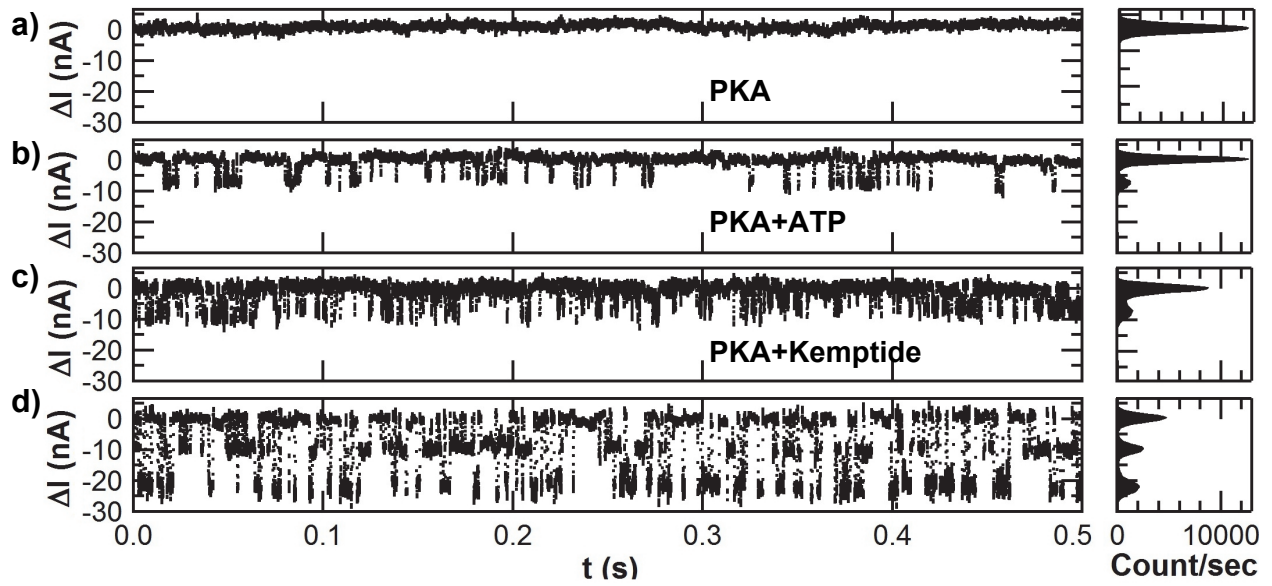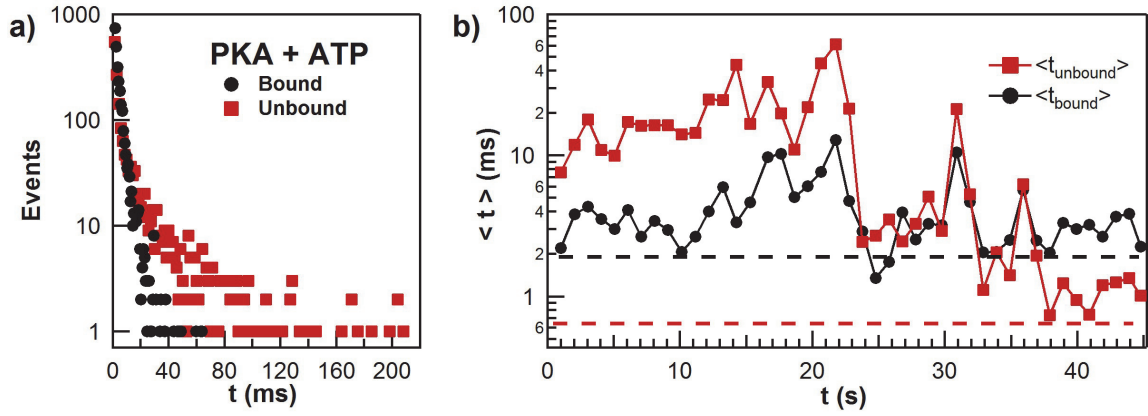Figure 4



Figure 5
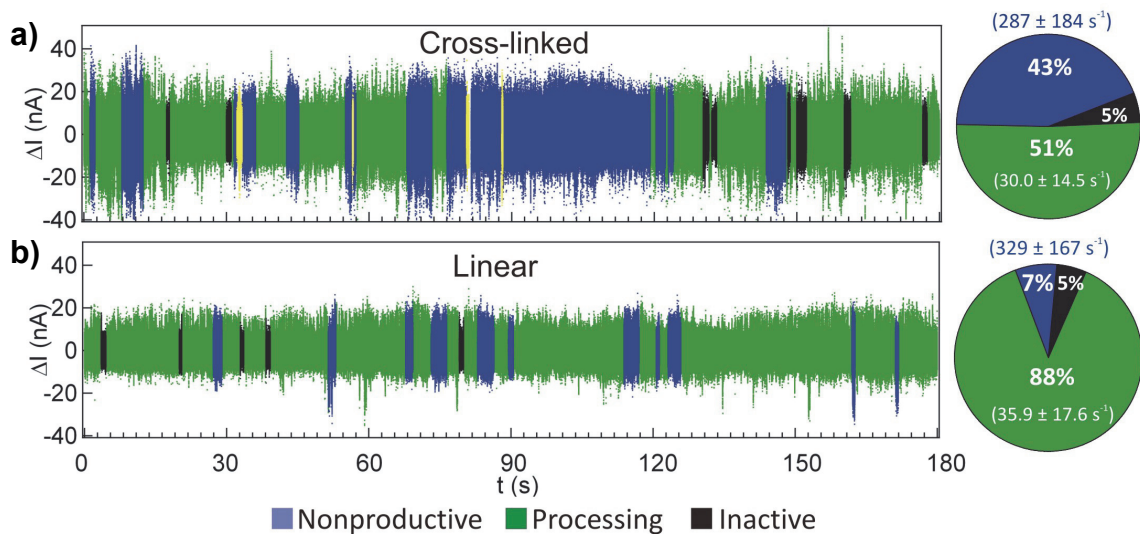
Figure 6
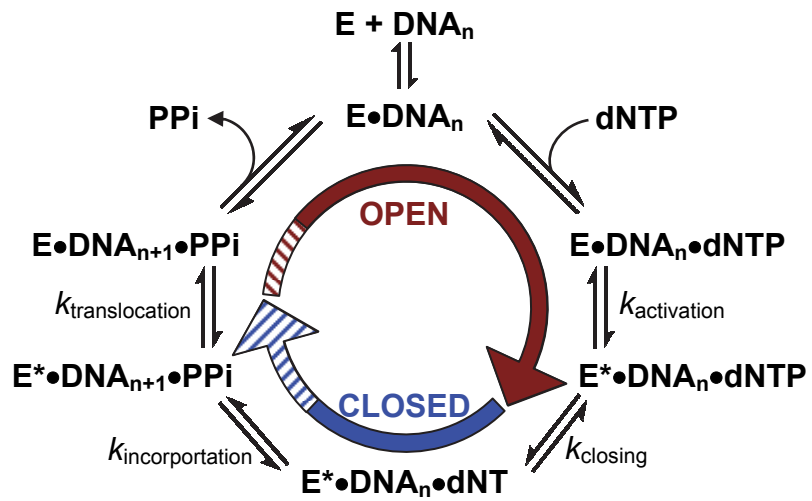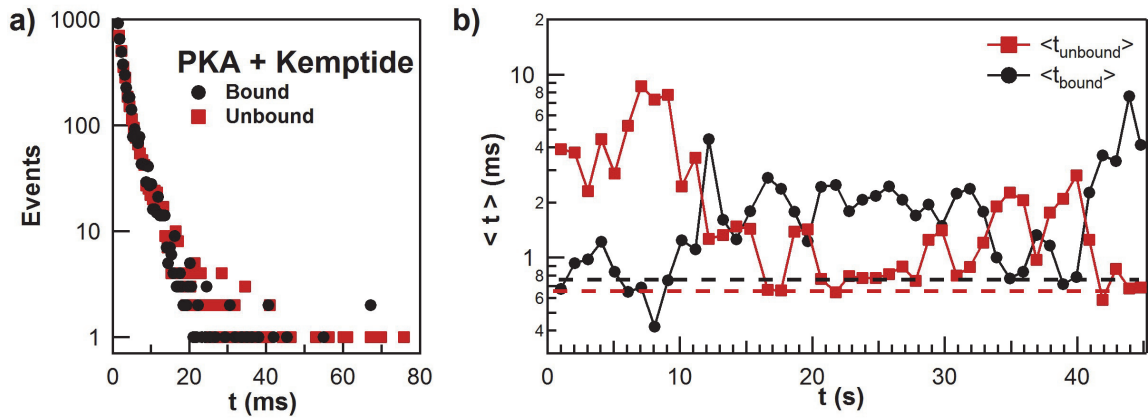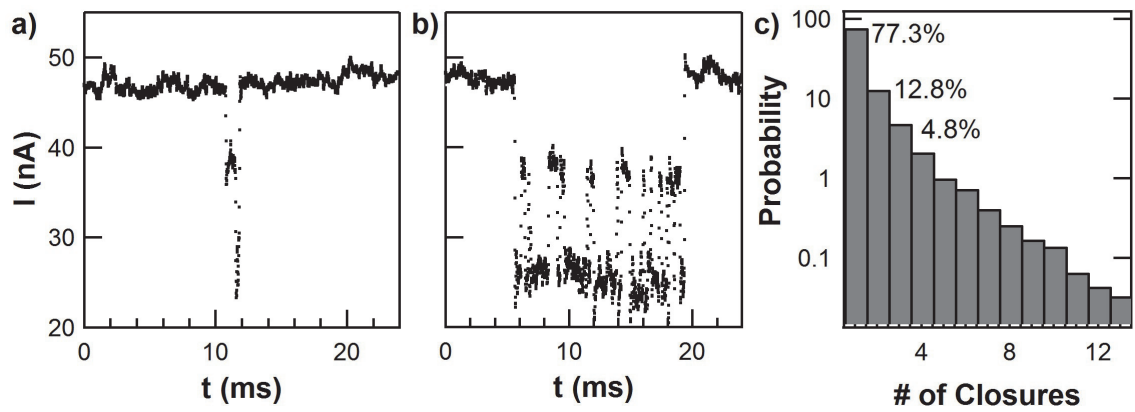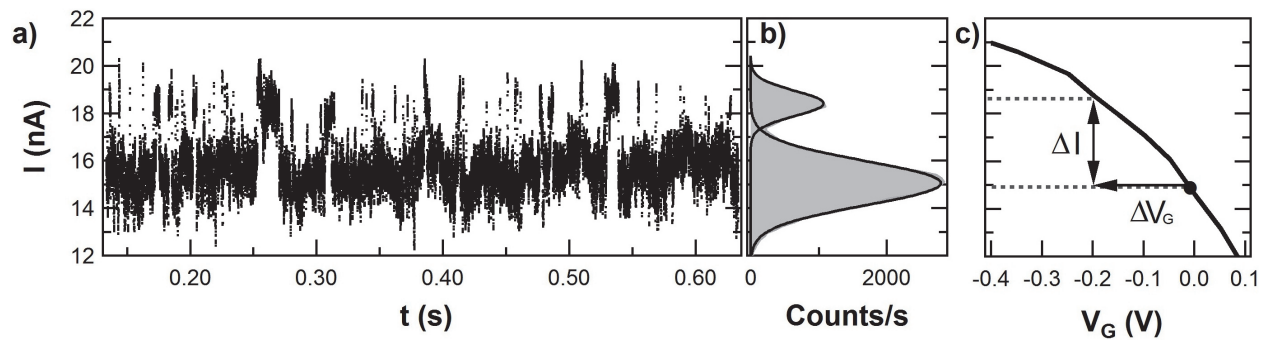


Figure 7

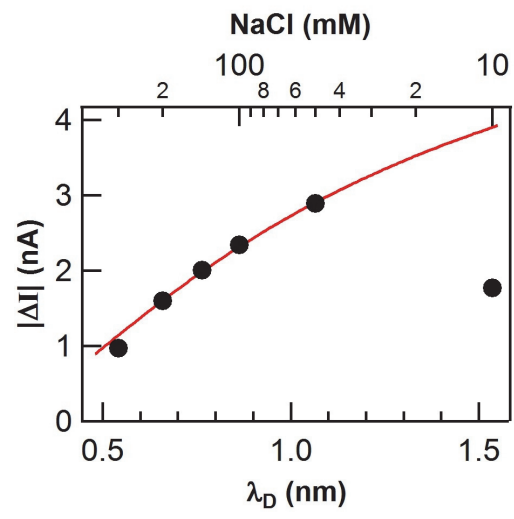Figure 8


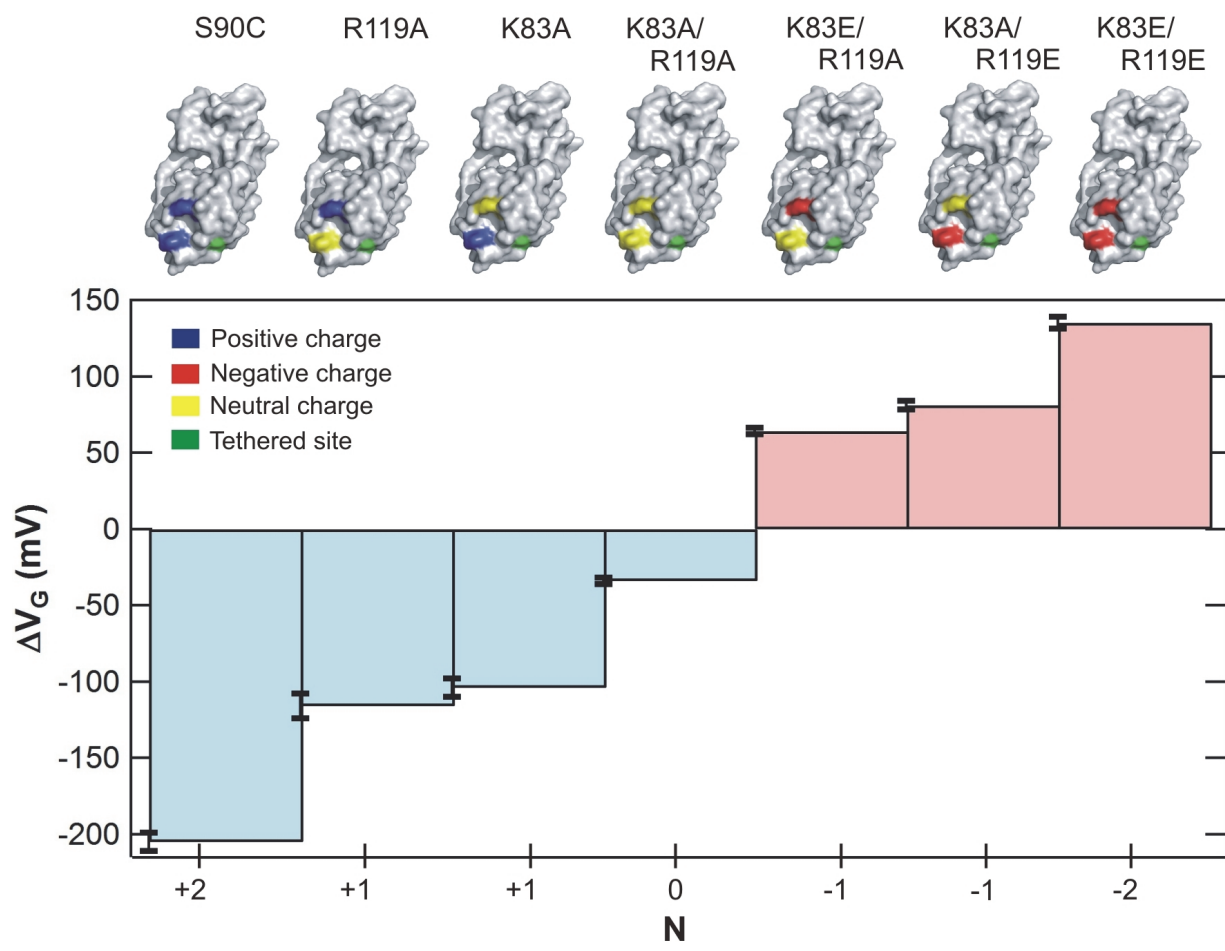
Figure 9

Figure 10



Figure 11

Figure 12



Figure 13



Figure 14

Figure 15



Figure 16

Figure 17